Inverted hysteresis as a diagnostic tool for perovskite solar cells: Insights from the drift-diffusion model

Will Clarke,[1] Matthew Cowley,[2, 3] Matthew Wolf,[4] Petra Cameron,[2, 3] Alison Walker,[5] and Giles Richardson[1]

[1] *Mathematical Sciences, University of Southampton, UK*
[2] *Centre for Sustainable and Circular Technologies, University of Bath, UK*
[3] *Department of Chemistry, University of Bath, UK*
[4] *Institute of Physical Chemistry, RWTH Aachen, Germany*
[5] *Department of Physics, University of Bath, UK*

Despite current-voltage hysteresis in perovskite solar cells (PSCs) having been the subject of significant research over the past decade, inverted hysteresis (IH), although frequently observed, is still not properly understood. Several mechanisms, based on numerical simulations, have been proposed to explain it but a satisfactory description of the underlying cause remains elusive. To rectify this omission we analyse a drift-diffusion model of a planar three-layer PSC, using asymptotic techniques, to show how inverted hysteresis comes about. The asymptotic analysis of the drift-diffusion model yields a simple approximate model that shows excellent agreement with numerical simulations of the full drift-diffusion model, provides fundamental insights into the causes of IH and reconciles the alternative explanations found in the literature. This approximate model is analysed further to isolate the material properties and external conditions that contribute to inverted hysteresis, and constitutes a diagnostic tool in which the appearance of IH can be used to infer properties of the cell.

Keywords: Inverted hysteresis · Perovskite solar cells · Drift-diffusion · Ion migration · Matched asymptotics

I. BACKGROUND

A. Development of PSCs

Perovskite solar cells (PSCs) have received tremendous attention from the photovoltaics community over the past decade, as their power conversion efficiencies (PCEs) have climbed to be comparable to that of silicon solar cells (see, *e.g.* [1]), the current market leader. In 2012, efficiencies began to cross the 10% threshold [2, 3], sparking a significant research effort in the understanding and development of these devices. PSCs quickly became the fastest growing PV technology in terms of PCE, with a current record of 25.7% [4]. Another attractive benefit of PSCs is the possibility of cheap large-scale manufacturing, enabled by a variety of fabrication methods, involving solution processing [5, 6] and vapour deposition [7], many of which can be performed at low temperatures [8]. Following world record-breaking advances in perovskite-silicon tandem cells, large scale commercial production has been planned for 2022 [9].

While the efficiencies of 'champion cells' have increased rapidly, significant challenges to the commercial development of these devices remain, including long-term stability, reliance on toxic materials, and understanding of the effects of ion motion on the optoelectronic performance [10, 11]. The electrical characterisation of PSCs using standard techniques is hampered by showing long-lived transients on timescales of several seconds to hours. Current-voltage (J-V) measurements (intended to show steady state performance), which are typically performed at constant sweep rates, are therefore dependent on the bias history of the cell, and lead to *so-called* current-voltage 'hysteresis', as first reported by Snaith *et al.* [12]. These measurements proceed first with a preconditioning step in which the cell is held at some constant voltage $V_{\mathrm{pre}} > V_{\mathrm{OC}}$, for a fixed length of time, followed by a voltage sweep in which the applied voltage is reduced to short-circuit (the reverse scan) and then a sweep back to V_{OC} (the forward scan). Typically a range of scan rates exhibit hysteresis, meaning there is a marked difference between the forwards and reverse current-voltage measurements [13]. Even so-called hysteresis-free cells will show hysteresis if a wide enough range of scan rates and temperatures are investigated.

The use of drift-diffusion (DD) models [14–18] offers a powerful tool to improve understanding of PSCs, guiding further development and providing theoretical insight to address some of the remaining challenges. Following the first observations of current-voltage hysteresis in PSCs, several mechanisms were proposed in the literature [19, 20]. Ion migration became the favoured candidate due to findings that halide ions were mobile on timescales matching those of hysteresis [21, 22]. Drift-diffusion models of electrons and holes are an established technique in semiconductor modelling [23, 24] and were used to test theories of ion migration in PSCs by incorporating slow-moving ionic species into the model [14, 15, 25]. This addition, however, introduces extreme spatial and temporal stiffness to the system, requiring tailored approaches to obtain accurate solutions. Stiff equations are those in which solutions undergo substantial variations over short timescales or over small spatial regions, and render many numerical techniques unstable. Temporal stiffness occurs due to the disparity in the timescales of motion of ionic (slow) and electronic (fast) species and spatial stiffness due to carrier accumulation in thin Debye layers

(∼ 1.5 nm) near interfaces, predicted by the high density of ion vacancies in the perovskite [15]. While early numerical approaches to solving the DD equations were not capable of solving for physical parameter sets [14], Courtier *et al.* [26] and Calado *et al.* [27] have both developed reliable numerical approaches without excessive computation times. In the former case the resulting finite element scheme has been made publicly available with the release of the open-source PSC simulation software, `IonMonger` [28] whilst in the latter it has been released as the open source code `Driftfusion`.

To avoid the computational difficulties of solving such stiff equations, a different approach was taken by Richardson *et al.* [15, 29] in which matched asymptotic analysis was employed to systematically obtain a simple approximate model (termed the surface polarisation model (SPM)), which accurately captures the behaviour of the underlying mixed-ionic drift diffusion model over a large portion of the physically relevant parameter space. In the SPM, ions are decoupled from electronic carriers in the perovskite (meaning the electric potential is determined solely by the ionic charge) and the cell is characterised by the charge density stored within the Debye layers near each material interface (discussed in more detail in Section III). Courtier *et al.* later extended the SPM to explicitly include the transport layers [16]. Although the SPM is not always as accurate as numerical solutions to the full DD model, the simplicity of the SPM provides significant additional insight into the mechanisms underlying PSC behaviour. Several other studies have also arrived at simplified models of PSCs that approximate the behaviour of the full DD model while offering greater insight, although none of them have been systematically derived from the underlying DD model (as the SPM has). Ravishankar *et al.* [30] developed a similar surface polarisation model, however the capacitance relation used for the ionic Debye layers is not compatible with the DD model and, in particular, results in a non-zero surface charge density at the perovskite/transport layer interfaces when the potential difference across these interfaces is zero. Moia *et al.* [31] obtained an equivalent circuit model comprising an ionically gated transistor-interface and Bertoluzzi *et al.* [32] provided an analytical model of the band diagrams loosely based on Richardson's surface polarisation model.

Whilst all four of these simplified models can be said to approximate the full PSC DD model in certain parameter regimes, none are capable of recreating the inverted hysteresis scans that are seen in numerical DD simulations (shown for the SPM in Figure 2) in certain parameter regimes and which are discussed in detail in the next section. It is the aim of this work to systematically extend the SPM, by deriving to regimes in which inverted hysteresis is observed.

B. Inverted hysteresis

A hysteretic current-voltage sweep usually exhibits greater current output throughout the reverse sweep (from open-circuit to short-circuit) than on the forward sweep (from short-circuit to open-circuit) [12, 21], sometimes referred to as normal hysteresis (NH). Some cells, however, have shown larger current output on the forward sweep than the reverse [33–35]. This has been termed inverted hysteresis (IH) [36, 37]. While a consensus has not been reached on an exact distinction between NH and IH, the latter includes a higher open-circuit voltage on the forward sweep and/or at least some region of the sweep in which the current output is greater on the forward sweep. Examples of both normal and inverted hysteresis are shown in Figure 1. Since the phenomenon
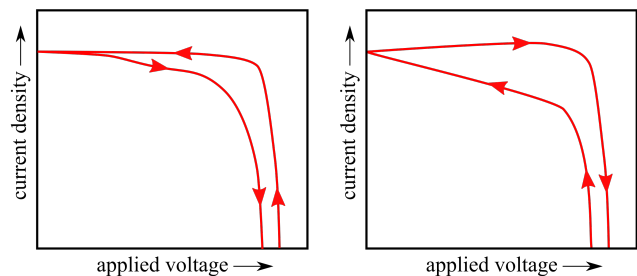

FIG. 1. Schematics of normal (left) and inverted (right) hysteresis.

was first observed, there have been attempts to replicate IH in simulations and models in order to understand the underlying cause, with some success (as discussed below). A consensus on the underlying mechanism has, however, not been reached.

Jacobs *et al.* reproduced IH in numerical drift-diffusion simulations [39], and suggest that preconditioning at voltages much larger than the cell's built-in voltage induced IH due to reverse accumulation of ion vacancies *i.e.* positive vacancies accumulate near the ETL, in contrast to normal operating conditions. However, their simulations were performed with ions immobilised in some pre-bias configuration, rather than being allowed to evolve in time, despite being conducted over timescales on which ions are likely to be mobile. This thus limits their ability to infer likely mechanisms for IH from experimental data.

Shen *et al.* [40] also replicated IH with numerical simulations but drew different conclusions from Jacobs *et al.* as to its underlying causes. In particular they discussed two possible mechanisms; the first based on band-bending and the second on accumulation of ionic charge in the perovskite bulk. They suggested that highly asymmetrical band alignment between the transport layers and the perovskite causes a significant population of electrons to build up within the perovskite, leading to it becoming n-type. And that any subsequent change to the applied voltage then affects the HTL/perovskite p-n junction, leaving the electric potential uniform over a
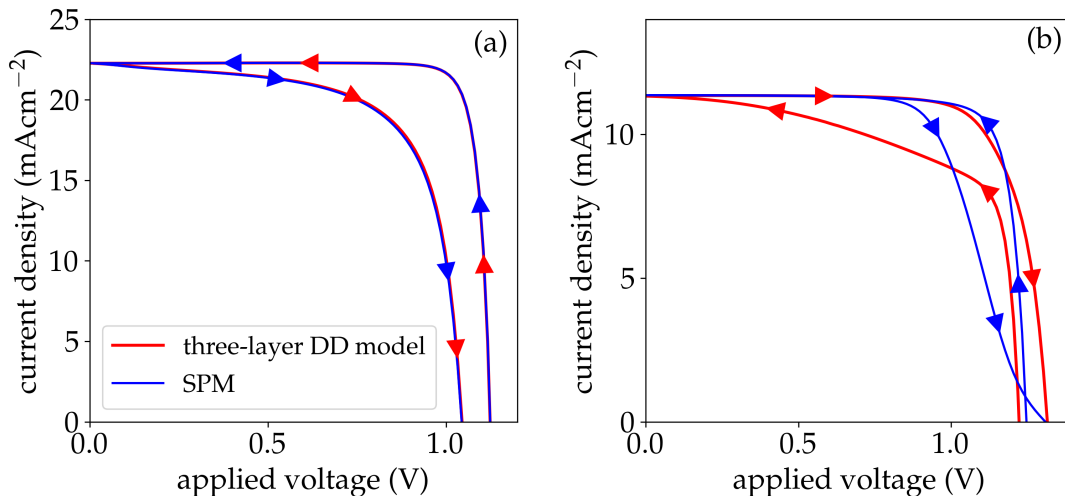
FIG. 2. Validation of the SPM against numerical solutions. Panel (a) shows the current-voltage curve for a 500mVs^{-1} sweep of the parameter set from Tables 3.2 and 3.3b of [38] that does not exhibit inverted hysteresis and represents a typical TiO_2/MAPI/spiro-MeOTAD cell while panel (b) shows a 50mVs^{-1} sweep of a parameter set shown to exhibit strong inverted hysteresis (listed in table S1 of the Supplementary Information) and representative of a PCBM/MAPI/NiO_x cell. Red lines are numerical solutions of the full three-layer drift-diffusion model obtained with the PSC simulation software `IonMonger` [28] and blue lines are numerical solutions of the SPM (Eq. 19 from [16]).

large region of the cell near the ETL interface. In this region, carrier transport is diffusion-limited, resulting in increased bulk recombination losses. The drift-diffusion model used explicit dynamic coupling of mobile ions to carriers and electric potential.

García-Rodríguez *et al.* used the PSC simulation tool, `IonMonger`, in conjunction with experimental data to investigate the role of cell architecture on IH [41].They found that IH can be observed in both p-i-n and n-i-p architectures and that hysteresis typically switches from normal to inverted as scan rate increases. The scan rates at which maximal normal and inverted hysteresis were shown to be sensitive to the ion vacancy diffusion coefficient, the ion vacancy density and the nature of the transport layer materials.

Recently, Gonzales *et al.* [42] identified a link between inverted hysteresis and the so-called negative capacitance feature frequently observed in impedance spectra of PSCs [43]. It was found that both phenomena can be well described by the addition of a 'chemical inductor' to the equivalent circuit model of a PSC. Despite being able to recreate experimental data, the equivalent circuit models were not derived systematically from the drift-diffusion equations, meaning the physical origin of each circuit element is unclear. Indeed, it was stated that the molecular origin of the chemical inductance has not yet been identified.

Another recent work by Minbashi and Yazdani [44] modified the drift-diffusion model to simulate IH, allowing mobile ions to cross material interfaces. However, two mobile ion species were assumed to have equal mobilities, a scenario shown to be unlikely by Bertoluzzi *et al.* [32]. As we shall show here, no additions to the

standard drift-diffusion model of PSCs are required to reproduce inverted hysteresis.

Although these studies [39–41] have shown that mixed-ionic drift-diffusion models are capable of exhibiting inverted hysteresis, their numerical simulations do not provide an unambiguous explanation of the underlying mechanism behind this phenomenon. The ambiguity can largely be attributed to the complexity of the mixed-ionic three-layer DD model. As discussed in the previous section, simplified models can offer additional insight into the behaviour of the full cell but none reported thus far are capable of recreating IH as observed in numerical simulations. In what follows we systematically derive a modified surface polarisation model (mSPM), from the mixed-ionic DD model, with the goal of elucidating the mechanisms that underlie inverted hysteresis. We begin, in Section II, by stating the familiar mixed-ionic three-layer drift-diffusion (DD) model of a perovskite solar cell. Section III includes a brief description of the standard surface polarisation model, as derived in Richardson *et al.* [15] and extended in Courtier *et al.* [16]. We show that while the SPM is very accurate for typical parameter sets, it performs poorly for parameter sets exhibiting inverted hysteresis, and this motivates modifications to the assumptions used to derive the SPM. The mSPM, and the assumptions on which it is based, are discussed in Section IV, where solutions are successfully validated against solutions of the full three-layer DD model. In Section V, we present further analysis of the problem under external conditions of preconditioning at a fixed voltage and a linear voltage sweep, obtaining a relation between timescales of inverted hysteresis and material parameters. Finally, in Section VI, we show that the mSPM

reconciles the partial explanations of IH put forward in the literature under a single, complete description and provides a pathway to use IH as a diagnostic tool, which can be used to help guide the design of cells with improved steady state performance.

II. THE DRIFT-DIFFUSION MODEL

We begin by stating the full drift-diffusion model of the three-layer planar PSC. This model (or minor variations of it) has been widely adopted and shown to accurately reproduce the current-voltage characteristics and impedance response of PSCs [15–18, 28, 29, 31, 45–47]. A perovskite absorber layer is sandwiched between an n-type electron transport layer (ETL) and a p-type hole transport layer (HTL). Both n-i-p and p-i-n architectures can be modelled by simply changing the direction of the light. A schematic of the cell is shown in Figure 3. In each layer, we model transport of each mobile charge species by a conservation equation coupled to a flux equation that is the sum of responses to gradients in electric potential (drift) and number density (diffusion). All charged species are then fully coupled to the electric potential via Poisson's equation. Ion motion is modelled explicitly, allowing for spatial and temporal variation.

A. The perovskite layer

In this layer we assume three mobile charged species: anion vacancies (P), electrons (n), and holes (p), with fluxes F^P, j^n, and j^p, respectively. The conservation equations and their corresponding fluxes are

$$\frac{\partial P}{\partial t} = -\frac{\partial F^P}{\partial x},$$
$$F^P = -D_P \left(\frac{\partial P}{\partial x} + \frac{q}{k_B T} P \frac{\partial \phi}{\partial x} \right), \quad (1)$$

$$\frac{\partial n}{\partial t} = \frac{1}{q} \frac{\partial j^n}{\partial x} + G - R,$$
$$j^n = q D_n \left(\frac{\partial n}{\partial x} - \frac{q}{k_B T} n \frac{\partial \phi}{\partial x} \right), \quad (2)$$

$$\frac{\partial p}{\partial t} = -\frac{1}{q} \frac{\partial j^p}{\partial x} + G - R,$$
$$j^p = -q D_p \left(\frac{\partial p}{\partial x} + \frac{q}{k_B T} p \frac{\partial \phi}{\partial x} \right). \quad (3)$$

Here G and R are the rates of electronic carrier generation and recombination respectively, forms of which are given in (27)-(31). The three charged species are coupled to the electric potential (ϕ) via Poisson's equation,

$$\frac{\partial^2 \phi}{\partial x^2} = \frac{q}{\varepsilon_p} (N_0 - P + n - p). \quad (4)$$

We have assumed a uniform background density (N_0) of immobile cation vacancies, following the findings of
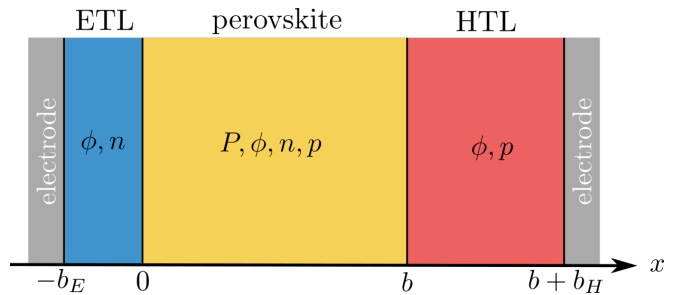

FIG. 3. Schematic of the planar PSC model. The continuum variables modelled in each layer are shown.

Bertoluzzi *et al.* [32]. Definitions of material parameter symbols and the values adopted can be found in Table S1 of the Supplementary Information.

B. The ETL

The electron transport layer is assumed to be highly n-doped. It is assumed that the hole density in this layer is negligible, as are the effects of carrier generation and recombination. In this region the model therefore comprises a single conservation equation for electrons,

$$\frac{\partial n}{\partial t} = \frac{1}{q} \frac{\partial j^n}{\partial x}, \quad (5)$$

coupled to the electron current density

$$j^n = q D_E \left(\frac{\partial n}{\partial x} - \frac{n}{V_T} \frac{\partial \phi}{\partial x} \right). \quad (6)$$

The electron density is also coupled to the electric potential via Poisson's equation,

$$\frac{\partial^2 \phi}{\partial x^2} = \frac{q}{\varepsilon_E} (n - d_E) \quad (7)$$

where d_E is the effective doping density, equal to the (uniform) density of donor atoms in the lattice. The ETL is assumed to form an Ohmic contact with the metal cathode, leading to the boundary conditions

$$n|_{x=-b_E} = d_E, \qquad \phi|_{x=-b_E} = -\frac{V(t) - V_{bi}}{2}, \quad (8)$$

where $V(t)$ is the voltage applied across the cell and

$$V_{bi} = \frac{1}{q} \left(E_c^E - E_v^H \right) - V_T \ln \left(\frac{g_c^E g_v^H}{d_E d_H} \right) \quad (9)$$

is the built-in voltage, equal to the difference in the equilibrium quasi-Fermi levels of the transport layers.

C. The HTL

Similarly, the minority carrier density in the highly p-doped HTL is assumed to be negligible, as are the effects

of carrier generation and recombination. The model in this region comprises a single equation for conservation of holes,

$$\frac{\partial p}{\partial t} = \frac{-1}{q}\frac{\partial j^p}{\partial x}, \tag{10}$$

coupled to the hole current density

$$j^p = -qD_H\left(\frac{\partial p}{\partial x} + \frac{p}{V_T}\frac{\partial \phi}{\partial x}\right). \tag{11}$$

The hole density is coupled to the electric potential via Poisson's equation,

$$\frac{\partial^2 \phi}{\partial x^2} = \frac{q}{\varepsilon_H}(d_H - p), \tag{12}$$

where d_H is the effective doping density, equal to the density of acceptor atoms in the lattice. The HTL is assumed to form an Ohmic contact with the metal anode, leading to the boundary conditions

$$p|_{x=b+b_H} = d_H, \qquad \phi|_{x=b+b_H} = \frac{V(t) - V_{bi}}{2}. \tag{13}$$

D. Interface Conditions

Electric potential, electric displacement field, and majority carrier QFL are assumed to be continuous across the material interfaces. Similarly, electronic currents are conserved over the interfaces and anion vacancies are confined to the perovskite layer, meaning the ion flux is zero on both interfaces. The resulting continuity conditions are

$$F^P|_{x=0} = 0, \tag{14}$$
$$j^p|_{x=0} = -qR_l, \tag{15}$$
$$j^n|_{x=0^-} = j^n|_{x=0^+} - qR_l, \tag{16}$$
$$\phi|_{x=0^-} = \phi|_{x=0^+}, \tag{17}$$
$$\varepsilon_E\frac{\partial \phi}{\partial x}|_{x=0^-} = \varepsilon_p\frac{\partial \phi}{\partial x}|_{x=0^+}, \tag{18}$$
$$k_E n_E|_{x=0^-} = n|_{x=0^+}, \tag{19}$$

at the ETL interface and

$$F^P|_{x=b} = 0, \tag{20}$$
$$j^n|_{x=b} = qR_r, \tag{21}$$
$$j^p|_{x=b^-} - qR_r = j^p|_{x=b^+}, \tag{22}$$
$$\phi|_{x=b^-} = \phi|_{x=b^+}, \tag{23}$$
$$\varepsilon_p\frac{\partial \phi}{\partial x}|_{x=b^-} = \varepsilon_H\frac{\partial \phi}{\partial x}|_{x=b^+}, \tag{24}$$
$$p|_{x=b^-} = k_H p_H|_{x=b^+}. \tag{25}$$

at the HTL interface. Here R_l and R_r are the rates of interfacial recombination at the ETL/perovskite and HTL/perovskite interfaces, respectively, in which majority carriers from the transport layers recombine with minority carriers from the perovskite. The ratios of majority carrier densities either side of the transport layer interfaces are determined by the band offsets between the adjacent materials,

$$k_E = \frac{g_c}{g_c^E}\exp\left(\frac{E_c^E - E_c}{k_B T}\right),$$
$$k_H = \frac{g_v}{g_v^H}\exp\left(\frac{E_v - E_v^H}{k_B T}\right). \tag{26}$$

E. Generation and recombination

The rate of carrier generation in the perovskite is assumed to follow the Beer-Lambert law of light absorption for a single wavelength and absorption coefficient,

$$G(x,t) = I_s(t)F_{ph}\alpha e^{-\alpha x}, \tag{27}$$

where F_{ph} is the incident photon flux, α is the perovskite absorption coefficient, and $I_s(t)$ is the light intensity. Note that this form of the generation rate assumes the cell has so-called normal architecture (light entering through the ETL). Inverted architectures, in which the light enters through the HTL, can be modelled with the generation rate $G(b - x, t)$. In this cell, bulk recombination is assumed to be dominated by Shockley-Read-Hall (SRH), the rate of which is given by

$$R(n,p) = \frac{np - n_i^2}{\tau_n p + \tau_p n + (\tau_n + \tau_p)n_i}. \tag{28}$$

The intrinsic carrier density in the perovskite is defined as

$$n_i^2 = g_c g_v \exp\left(\frac{E_v - E_c}{k_B T}\right). \tag{29}$$

Interfacial recombination is assumed to be dominated by SRH recombination with rates

$$R_l = \frac{np - n_i^2}{\frac{k_E}{\nu_{n,E}}p + \frac{1}{\nu_{p,E}}n + \left(\frac{k_E}{\nu_{n,E}} + \frac{1}{\nu_{p,E}}\right)n_i}, \tag{30}$$

$$R_r = \frac{np - n_i^2}{\frac{1}{\nu_{n,H}}p + \frac{k_H}{\nu_{p,H}}n + \left(\frac{1}{\nu_{n,H}} + \frac{k_H}{\nu_{p,H}}\right)n_i}. \tag{31}$$

III. THE SURFACE POLARISATION MODEL

While the drift-diffusion (DD) model detailed in the previous section can be solved numerically [27, 28], deeper physical insight may be gained from approximating the model, in relevant parameter regimes, using asymptotic methods to obtain a simpler, albeit slightly less accurate, model which is more readily analysed. Many PSCs have physical parameter values for which the
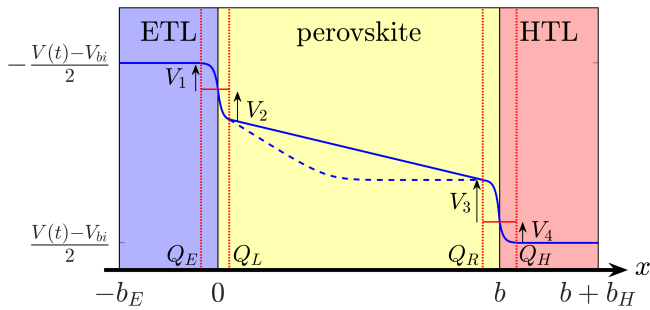
FIG. 4. Electric potential in the SPM. The dashed line shows the adaption to the modified SPM.

DD model is well-approximated by the so-called Surface Polarisation Model (SPM) (see [15, 16, 29]) such that their behaviour is accurately captured by this much simpler model. In this section we give a brief overview of the SPM and discuss its validity for parameter sets that exhibit inverted hysteresis.

The large densities of the dominant mobile charge species in each layer (ion vacancies in the perovskite, electrons in the ETL, holes in the HTL) lead to Debye lengths much smaller than the width of each layer. This motivated Richardson *et al.* [15, 29] to apply the method of matched asymptotic expansions to the DD model. In the case of a planar cell with three-layers, as depicted in Fig. 4, this leads to a solution with a seven layer structure (see Ref. [16] and Figure 4) consisting of four narrow boundary layer regions (the so-called Debye layers) that lie adjacent to the interfaces between the perovskite absorber layer and the transport layers and three bulk regions that lie away from these interfaces. In the Debye layers there is significant charge accumulation whilst in the bulk regions there is almost exact charge neutrality.

The systematic derivation of the SPM from the drift-diffusion equations relies on five key assumptions:

i The Debye length in the perovskite, defined by $L_D = \sqrt{\frac{\varepsilon_p V_T}{q N_0}}$, is small in comparison to the width of the perovskite layer, $\frac{L_D}{b} = \mathcal{O}(10^{-3})$.

ii Electron and hole densities in the perovskite layer are very much smaller than that of the mobile ions.

iii The timescale for electronic carrier motion is very much faster than that of ion motion in the perovskite.

iv The Debye lengths of electrons and holes in their respective transport layers are much smaller than the widths of the transport layers.

v The electronic carriers in the transport layers are highly mobile.

Under these assumptions, the electric potential is found to be linear throughout each of the three bulk layers, a consequence of near total charge neutrality in these regions. Furthermore, each of the Debye layers can be characterised by the surface charge density that it stores (for the four layers, proceeding from left to right, these are denoted by Q_E, Q_L, Q_R and Q_H, respectively) and the potential drop across it (V_1, V_2, V_3 and V_4, respectively). The charge density in the perovskite Debye layers is dominated by anion vacancies, accumulating near one interface and depleting from the other. Confining these vacancies to the perovskite layer and assuming a constant uniform background density of immobile cation vacancies leads to a condition of net neutrality on the perovskite Debye layers, $Q_L = -Q_R$. Similarly, applying continuity of displacement electric field across the two interfaces leads to the relations $\mathcal{Q}_E = -\mathcal{Q}_L$ and $\mathcal{Q}_H = -\mathcal{Q}_R$. This allows $\mathcal{Q}_E$, $\mathcal{Q}_L$, and $\mathcal{Q}_H$ to be eliminated in favour of $\mathcal{Q}_R$, and results in a single ODE for $\mathcal{Q}_R$, the charge density stored in the right-hand perovskite Debye layer,

$$\frac{dQ_R}{dt} = \frac{q N_0 D_P}{b k_B T}\left(V_{bi} - V(t) - V_1 - V_2 - V_3 - V_4\right),$$

(Eq. 19 from [16])

where

$$\begin{array}{ll} V_1 = -\mathcal{V}(-\Omega_E \mathcal{Q}_R), & V_2 = -\mathcal{V}(-\mathcal{Q}_R), \\ V_3 = \mathcal{V}(\mathcal{Q}_R), & V_4 = -\mathcal{V}(-\Omega_H \mathcal{Q}_R), \end{array} \quad (32)$$

are the potential drops over each of the Debye layers, $\mathcal{V}(\mathcal{Q})$ is the non-linear capacitance relation of the Debye layers, defined as the inverse of

$$\mathcal{Q}(\mathcal{V}) = \sqrt{q N_0 \varepsilon_p V_T}\,\mathrm{sign}(\mathcal{V})\sqrt{2\left(e^{\mathcal{V}/V_T} - \mathcal{V}/V_T - 1\right)},$$

(33)

and $\Omega_E = \frac{\varepsilon_p N_0}{\varepsilon_E d_E}$ and $\Omega_H = \frac{\varepsilon_p N_0}{\varepsilon_H d_H}$ are non-dimensional constants that determine how the potential difference across the device is divided between the three layers. Once a time-dependent solution for Q_R has been obtained through numerical solution of the ODE, the current density can be found through solutions of carrier densities in the perovskite bulk on the background electric potential.

Current-voltage curves obtained from the SPM are shown against numerical solutions in Figure 2. As was shown by Courtier *et al.* [29], the SPM shows excellent agreement with numerical results for typical parameter sets that do not exhibit IH (Figure 2a), and provides significant insight into the behaviour of the complex three-layer drift-diffusion model. However, the model shows poor agreement with numerical solution to the full drift-diffusion model for parameter sets that exhibit IH (Figure 2b) and the understanding of PSCs built upon the SPM needs to be revised in these cases.

IV. THE MODIFIED SURFACE POLARISATION MODEL

Numerical simulations exhibiting IH typically show a large density of one species of electronic carrier in the

perovskite bulk before the sweep begins [40, 41], a feature not usually seen in simulations showing normal hysteresis. Motivated by the link between inverted hysteresis and large carrier densities, we present the modified surface polarisation model (mSPM), in which the asymptotic assumptions of the SPM are altered to reflect this carrier population and the systematic analysis of the drift-diffusion equations is repeated with the updated assumptions. In this section, the mSPM is briefly outlined in terms of dimensional variables. The full systematic derivation from the drift-diffusion equations is given in the Supplementary Information.

The typical ratios of electrons and holes to anion vacancies in the perovskite bulk in steady state conditions are given by

$$\frac{n}{P} \approx \frac{d_E g_c}{N_0 g_c^E} \exp\left(\frac{E_c^E - E_c - V_1 - V_2}{V_T}\right), \quad (34)$$

$$\frac{p}{P} \approx \frac{d_H g_v}{N_0 g_v^H} \exp\left(\frac{E_v - E_v^H - V_3 - V_4}{V_T}\right), \quad (35)$$

where $V_1 - V_4$ are the potential drops illustrated in Fig. 4 and the parameters in this expression are as defined in Table S1 of the Supplementary Information. In the standard SPM, the assumption is that both electron and hole densities are sufficiently small that they do not contribute significantly to the net charge density across the perovskite layer (including the Debye layers at its edges). The electron and hole problems thus decouple, at leading order, from the ion problem (reflected in assumption ii in §III). As discussed in the previous section, numerical simulations suggest that this assumption is not justified for parameter sets that exhibit IH due to the presence of significantly larger carrier densities. Here we shall assume that only one of the electron and hole densities is sufficiently small that it can be neglected from the overall charge density across the perovskite layer and that it is the other charge carrier that has a significant effect on the evolution of the ion density. When preconditioning at voltages larger than V_{bi} (as is common protocol), ion vacancies migrate away from the HTL, leaving a depletion region near the interface [29]. Due to the asymmetry of the Debye layer capacitance relation (Figure S1 of the Supplementary Information), a greater potential drop occurs across depletion regions than accumulation regions. This presents holes with a greater extraction barrier than electrons. For this reason, the carrier imbalance is assumed to favour holes over electrons. This manifests itself as an alteration to asymptotic assumption iii, which now becomes

iii The hole density in the perovskite bulk is much greater than the electron density, but much less than that of mobile anion vacancies, and the overall contribution to the charge density from holes in the perovskite layer is significant.

The inverse scenario, in which electrons outnumber holes during preconditioning, is discussed in the Supplementary Information.

In the Supplementary Information, we generalise the systematic asymptotic approach, adopted in [15, 16, 29] to derive the SPM from the DD model, to this new scenario. The results of this analysis show that, while the Debye layers are still characterised by the same capacitance relation (33), the electric potential (ϕ) is no longer approximately linear (i.e. it is no longer true that the electric field is spatially uniform) in the central (bulk) region of the perovskite (i.e. away from the Debye layers on the edges of the perovskite). Instead, ϕ satisfies the the following PDE in this region:

$$D_P N_0 \frac{\partial^2 \phi}{\partial x^2} = \frac{d_H g_v}{g_v^H} \exp\left(\frac{V(t) - V_{bi} - 2\phi}{2V_T} + \frac{E_v - E_v^H}{qV_T}\right) \frac{\partial}{\partial t}\left(\phi - \frac{V(t)}{2}\right) - \frac{\varepsilon_P V_T}{q} \frac{\partial}{\partial t}\left(\frac{\partial^2 \phi}{\partial x^2}\right), \quad (36a)$$

which couples to the perovskite Debye layer charge densities via the ODEs

$$\frac{dQ_L}{dt} = \frac{qD_P N_0}{V_T} \frac{\partial \phi}{\partial x}\Big|_{x=0^+}, \quad (36b)$$

$$\frac{dQ_R}{dt} = -\frac{qD_P N_0}{V_T} \frac{\partial \phi}{\partial x}\Big|_{x=b^-}, \quad (36c)$$

and satisfies the boundary conditions

$$\phi|_{x=0^+} = -\frac{V(t) + V_{bi}}{2} - V_1 - V_2, \quad (36d)$$

$$\phi|_{x=b^-} = \frac{V(t) + V_{bi}}{2} + V_3 + V_4, \quad (36e)$$

where the Debye layer potential drops are functions of the Debye layer charge densities, given by the capacitance relation (33)

$$V_1 = -\mathcal{V}(\Omega_E \mathcal{Q}_L), \quad V_2 = -\mathcal{V}(\mathcal{Q}_L), \quad (36f)$$

$$V_3 = \mathcal{V}(\mathcal{Q}_R), \quad V_4 = -\mathcal{V}(-\Omega_H \mathcal{Q}_L). \quad (36g)$$

Note that, in contrast to the standard SPM model, it is not in general true that $\mathcal{Q}_L = -\mathcal{Q}_R$; this is because the charge arising from the holes in the perovskite layer is significant and therefore affects the overall charge balance in this layer.

While this system cannot, in general, be solved analytically, the complexity of the full three layer drift-diffusion model has been greatly reduced, retaining only the leading order processes. Further analysis on this system under specific external conditions of interest will be presented in §V. Alternatively, this reduced system can
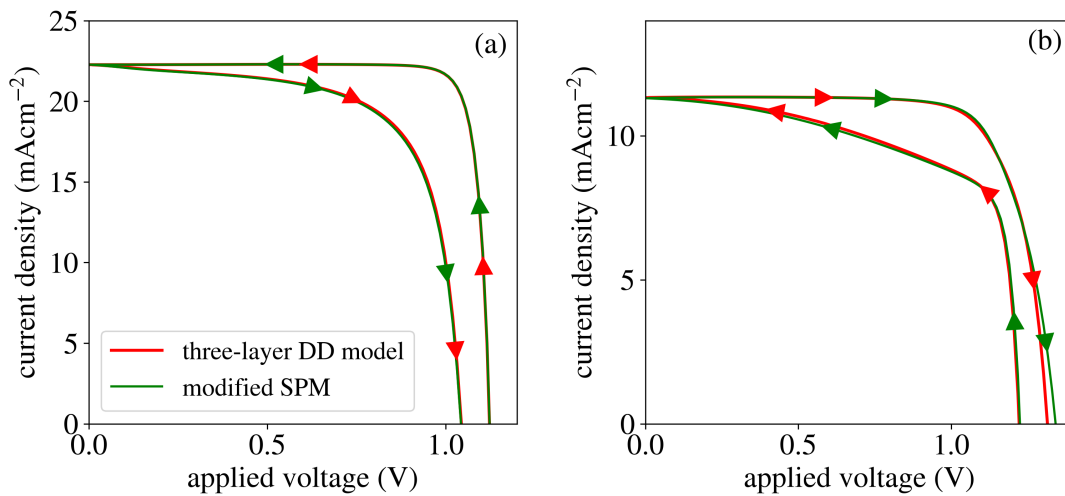
FIG. 5. Validation of the modified SPM against numerical solutions. As in Figure 2, panel (a) shows the current-voltage curve for a 500mVs^{-1} sweep of the parameter set from Tables 3.2 and 3.3b of [38] that does not exhibit inverted hysteresis and represents a typical TiO_2/MAPI/spiro-MeOTAD cell while panel (b) shows a 50mVs^{-1} sweep of a parameter set shown to exhibit strong inverted hysteresis (listed in Table S1 of the Supplementary Information) and representative of a PCBM/MAPI/NiO_x cell. Red lines are numerical solutions of the full three-layer drift-diffusion model obtained with the PSC simulation software `IonMonger` [28] and green lines are numerical solutions of the modified SPM (36).

easily be solved numerically with a suitable PDE solver as the severe spatial and temporal stiffness of the DD systems is removed by the boundary layer analysis of the Debye layers that gives rise to (36b)-(36e), and the assumption that electronic carriers are in a quasi-steady state (asymptotic assumption v).

In order to validate the modified SPM (36), we first consider the example of a current-voltage sweep at 50mVs^{-1} after the cell has reached steady state at a preconditioning voltage of 1.4V. The scan rate was chosen as it shows significant inverted hysteresis for this parameter set, which corresponds to a p-i-n cell with a PCBM/MAPI/NiO_x structure (listed in Table 1 of the Supplementary Information). Solutions to the modified SPM are compared against numerical solutions to the full three-layer drift-diffusion model obtained using `IonMonger` [28]. Figure 5b shows the current-voltage curve produced by the modified SPM plotted against a numerical solution of the full three-layer model. The mSPM shows excellent agreement with the numerical solution. In addition to being able to predict the behaviour of the J-V hysteresis curves, quantitative properties, such as the forward V_{OC}, reverse V_{OC}, and the short-circuit current are accurately predicted by the modified SPM, with relative errors of 0.69%, 0.32%, and 1.50%, respectively. However, the standard SPM (shown in Figure 2b) performs poorly, failing to replicate even the qualitative shape of the J-V curve. We also note that the mSPM is capable of reproducing normal hysteresis to the same accuracy as the already-validated SPM (Figure 5a).

Solutions to the electric potential during a reverse voltage sweep are shown in Figure 6, where they are compared against numerical solutions to the full three-layer
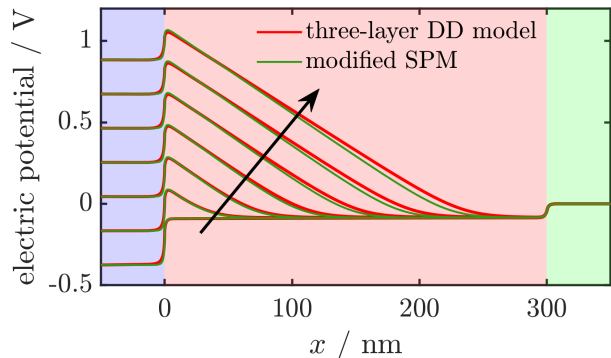

FIG. 6. Solutions of the electric potential during the 50mVs^{-1} reverse sweep of a PCBM/MAPI/NiO_x parameter set that exhibits strong inverted hysteresis (see Table 1 of the Supplementary Information). Red lines correspond to numerical solutions from `IonMonger` and green lines to numerical solutions of the modified SPM (36). The arrow shows the direction of increasing time. Note that here electric potential has been shifted by a time-dependent function such that the right hand boundary condition is now $\phi|_{x=b+b_H} = 0$ in order to more clearly show the behaviour of the solution.

DD model. Once again, excellent agreement is seen. While solutions from the standard SPM are not shown, the assumption that the electric potential is linear (i.e. the electric field $E(t)$ is spatially uniform) in the perovskite bulk is clearly not accurate in this case. This confirms that the underlying mechanism of inverted hysteresis that is displayed by this parameter set cannot be explained by the SPM, but requires the additional effects
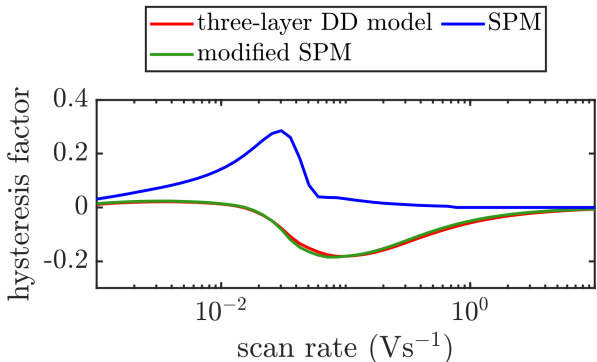
FIG. 7. Hysteresis factor (37) as a function of scan rate from three methods of solution. The red line shows full numerical solutions using `IonMonger`, the blue shows solutions of the SPM, and the green shows the modified SPM.

of a large hole population in the perovskite bulk.

The excellent agreement between the modified SPM and numerical solutions is not restricted to this single scan rate, but extends across the entire range of hysteretic scan rates. This is shown in Figure 7, where hysteresis factor is shown as a function of scan rate as predicted by the three methods of solution. Once again, the modified SPM performs very well, while the standard SPM does not, failing to predict a non-negligible negative hysteresis factor at any scan rate. While the hysteresis factor, defined by

$$ \text{HF} = \frac{\int_{V_{\min}}^{V_{OC}} (J_{\text{rev}} - J_{\text{for}}) dV}{\int_{V_{\min}}^{V_{OC}} J_{\text{rev}} dV}, \tag{37} $$

obscures much of the information regarding the nature of the hysteresis [37, 48] and should not be used as the only measure of hysteresis, it does offer convincing evidence that the modified SPM can be considered accurate across a broad range of scan rates.

V. ANALYSIS

The modified SPM is a much simpler model of a PSC than the full DD model, and predicts its behaviour from a single non-stiff PDE for the electric potential ($\phi(x,t)$) in the perovskite bulk coupled to two ODEs for the charge densities ($\mathcal{Q}_L(t)$ and $\mathcal{Q}_R(t)$) in the Debye layers. Furthermore numerical solutions to the modified SPM show close agreement (in the relevant regimes) to those of the full DD model. In this section, we further analyse the modified SPM to obtain a travelling wave solution which accurately describes the reverse sweep of a hysteresis experiment and can be used to explain the phenomenon of inverted hysteresis. Standard procedure for these measurements is to precondition the cell at some voltage $V^{\text{pre}} > V_{OC}$ until steady state is reached, then linearly sweep the applied voltage to short-circuit and back at

some fixed rate [33, 36, 40]. This motivates us to look for a solution that starts from steady state at $V = V^{\text{pre}}$ and then evolves in response to a linearly decreasing applied voltage.

A. Preconditioning

To investigate the behaviour of the mSPM during the preconditioning stage, we look for steady-state solutions of the modified SPM at some applied voltage V^{pre}. Steady-state is enforced by setting all time derivatives in the governing equations (36a-c) to be equal to zero. Under these conditions, the electric potential solution in the perovskite bulk is flat, (*i.e.* independent of x),

$$ \phi^{\text{pre}} = \frac{V^{\text{pre}} - V_{bi}}{2} + V_3^{\text{pre}} + V_4^{\text{pre}} \tag{38} $$

where $V_{1,\dots,4}^{\text{pre}}$ are the four Debye layer potential drops, determined by the Debye layer charge densities ($\mathcal{Q}_L^{\text{pre}}, \mathcal{Q}_R^{\text{pre}}$) according to (36f)-(36g). As no potential difference occurs across any of the bulk regions, the sum of the Debye layer potential drops must equal the total potential across the cell,

$$ V_1^{\text{pre}} + V_2^{\text{pre}} + V_3^{\text{pre}} + V_4^{\text{pre}} = V_{bi} - V^{\text{pre}}. \tag{39} $$

A third constraint is required to completely solve the system, provided by a statement of conservation of ionic charge. While the drift-diffusion equations require the total ionic charge in the perovskite to be constant, we also require ionic net neutrality, a condition usually supplied by initial conditions for the problem. This condition of ionic charge conservation and neutrality takes the form

$$ \int_0^b (P - N_0) dx = 0. \tag{40} $$

This third constraint shows that (unlike in the standard SPM) the ionic charge densities stored in the two perovskite Debye layers are not necessarily equal and opposite and depend on the preconditioning voltage,

$$ \mathcal{Q}_L^{\text{pre}} + \mathcal{Q}_R^{\text{pre}} = q d_H k_H b \exp \left(\frac{V^{\text{pre}} - V_{bi} + V_1^{\text{pre}} + V_2^{\text{pre}}}{V_T} \right). \tag{41} $$

This is caused by large hole densities flooding the perovskite when the preconditioning voltage is high. This accumulation of positive charge in the bulk forces anion vacancies to move from the bulk into the Debye layers, disturbing their net neutrality. Both the anion vacancy density and the hole density are uniform in the perovskite bulk being given by the expressions

$$ P^{\text{pre}} = N_0 - \frac{1}{bq} \left(\mathcal{Q}_L^{\text{pre}} + \mathcal{Q}_R^{\text{pre}} \right), \tag{42} $$

$$ p^{\text{pre}} = \frac{1}{bq} \left(\mathcal{Q}_L^{\text{pre}} + \mathcal{Q}_R^{\text{pre}} \right). \tag{43} $$

B. Analysis of the reverse sweep

The preconditioning step results in the cell reaching a steady state in which a large hole population in the perovskite bulk pushes ion vacancies from the bulk into the Debye layers. Here, the voltage scan from this preconditioning towards short-circuit conditions is considered. When a change occurs in the applied voltage, the electric field takes some finite time to permeate through the entire perovskite layer, seen in the time dependence of (36). To analyse the motion of the electric field through the device, we non-dimensionalise as follows:

$$x^* = \frac{x}{b}, \qquad t^* = \frac{t}{\tau_{\text{ion}}}, \qquad \phi^* = \frac{\phi}{V_T}, \qquad (44a)$$

$$\mathcal{Q}_{L,R}^* = \frac{\mathcal{Q}_{L,R}}{\sqrt{qN_0\varepsilon_p V_T}}, \qquad \mathcal{V}_{1,\dots,4}^* = \frac{V_{1,\dots,4}}{V_T}. \qquad (44b)$$

Here τ_{ion}, the typical timescale of ion vacancy motion, is defined by

$$\tau_{\text{ion}} = \frac{b}{D_P}\sqrt{\frac{V_T\varepsilon_p}{qN_0}}. \qquad (45)$$

Henceforth, the asterisk, denoting a dimensionless variable, is dropped as all quantities in what follows (unless otherwise stated) are dimensionless. In addition, we define φ, the shifted electric potential, by

$$\varphi = \phi - \phi^{\text{pre}} - \frac{\Phi(t) - \Phi^{\text{pre}}}{2} \qquad (46)$$

where $\Phi(t) = V(t)/V_T$ denotes the dimensionless applied voltage , and the superscript 'pre' denotes a quantity from the steady-state preconditioning solution. Note that ϕ^{pre} is the spatially independent electric potential in the perovskite bulk from the steady state reached during preconditioning.

After applying these scaling factors, the dimensionless governing equations of the modified SPM (36) become

$$\frac{d\mathcal{Q}_L}{dt} = \frac{\partial\varphi}{\partial x}\Big|_{x=0}, \qquad (47a)$$

$$m_p\lambda\alpha e^{-\varphi}\frac{\partial\varphi}{\partial t} - \lambda\frac{\partial}{\partial t}\left(\frac{\partial^2\varphi}{\partial x^2}\right) = \frac{\partial^2\varphi}{\partial x^2}, \qquad (47b)$$

$$\frac{d\mathcal{Q}_R}{dt} = -\frac{\partial\varphi}{\partial x}\Big|_{x=1}, \qquad (47c)$$

and satisfy the boundary conditions

$$\varphi|_{x=0} = \psi_0(t), \qquad \varphi|_{x=1} = \psi_1(t), \qquad (47d)$$

where

$$\psi_0(t) = -\Phi(t) + \Phi_{bi} - \mathcal{V}_1 - \mathcal{V}_2 - \mathcal{V}_3^{\text{pre}} - \mathcal{V}_4^{\text{pre}} \qquad (47e)$$
$$\psi_1(t) = \mathcal{V}_3 + \mathcal{V}_4 - \mathcal{V}_3^{\text{pre}} - \mathcal{V}_4^{\text{pre}}. \qquad (47f)$$

The three dimensionless constants appearing in equation 47b are defined as follows:

$$\lambda = \frac{1}{b}\sqrt{\frac{V_T\varepsilon_p}{qN_0}}, \qquad (48a)$$

$$m_p = \frac{d_H b^2 q g_v}{V_T\varepsilon_p g_v^H}\exp\left(\frac{E_v - E_v^H}{qV_T}\right), \qquad (48b)$$

$$\alpha = \exp\left(-\frac{V_3^{\text{pre}} + V_4^{\text{pre}}}{V_T}\right), \qquad (48c)$$

Here λ corresponds to the ratio of the Debye length to the width of the perovskite layer, m_p to the typical ratio of holes to ion vacancies, and α is a factor that measures how easily holes can enter the perovskite from the HTL during the preconditioning step. *The ratio of holes to ion vacancies, m_p, is of particular importance as it is this that determines the susceptibility of the cell to inverted hysteresis in terms of material parameters.*

The cell is in steady-state at the preconditioning voltage for times $t < 0$. The commencement of the voltage sweep, which starts at $t = 0$, perturbs the cell from its steady-state. The steady-state preconditioning solutions found in the previous section are used to determine initial conditions for (47) and, in particular, lead to the conditions $\psi_0(0) = \psi_1(0) = 0$.

From the boundary conditions (47e) and (47f), it is clear that a decrease in the applied voltage will manifest itself as an increase in φ at the left-hand boundary of the perovskite bulk, inducing a positive electric field in this region. Due to the nonlinear diffusion of φ, this electric field takes a finite time to permeate through the perovskite layer. Until the field reaches the right hand boundary, $\mathcal{Q}_R$ (and consequently $\mathcal{V}_3$ and $\mathcal{V}_4$) remain constant and equal to their values in the preconditioning step. During this period, the right hand boundary condition on φ is therefore $\psi_1(t) = 0$.

1. Travelling wave solutions

Numerical solutions to this problem show the solution split into three regions: two large linear regions connected by a thin internal-boundary-layer region that migrates from left to right across the perovskite layer, as shown in Figure 8. Motivated by these results, we investigate this solution using matched asymptotic expansions. In the two outer regions, $\frac{\partial^2\phi}{\partial x^2}$ is small, such that the left and right hand outer solutions are, to leading order,

$$\varphi^L = \psi_0(t) - E^L(t)x, \qquad (49)$$
$$\varphi^R = \psi_1(t) - E^R(t)(x - 1), \qquad (50)$$

respectively, where E^L and E^R are the electric field strengths in these regions, which are determined by matching to the inner (internal-boundary-layer) solution. Furthermore, numerical solutions imply that the electric
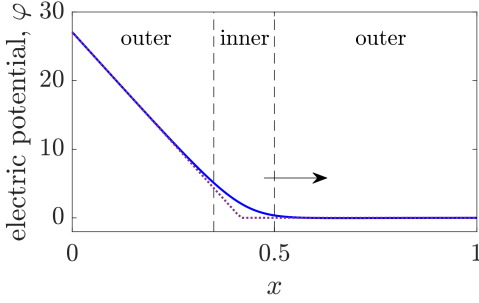
FIG. 8. The three regions of the solution to (47b) during the reverse sweep. The blue line is a numerical solution to (47b) and the purple dotted line shows an extrapolation of the two outer solutions into the boundary region. Arrow shows the direction of motion of the inner region.

potential in the right hand outer solution remains flat which suggests that $E^R(t) = 0$.

We assume that the boundary region is of width ϵ, where $\epsilon \ll 1$ and will be determined as part of the solution, and that it migrates at a speed c, starting from the left-hand boundary ($x = 0$) at $t = 0$. This motivates us to expand Equation (47b) about the point $x = ct$ (the location of the internal-boundary layer) and write the problem in the stretched travelling wave coordinates

$$\hat{x} = \frac{x - ct}{\epsilon}, \qquad \hat{t} = t. \qquad (51)$$

Under this transformation, (47b) becomes

$$\frac{\epsilon}{\lambda c}\frac{\partial^2 \varphi}{\partial \hat{x}^2} = \frac{m_p \alpha \epsilon^3}{c} e^{-\varphi}\frac{\partial \varphi}{\partial \hat{t}} - m_p \alpha \epsilon^2 e^{-\varphi}\frac{\partial \varphi}{\partial \hat{x}}$$
$$- \frac{\epsilon}{c}\frac{\partial}{\partial \hat{t}}\left(\frac{\partial^2 \varphi}{\partial \hat{x}^2}\right) + \frac{\partial^3 \varphi}{\partial \hat{x}^3}. \quad (52)$$

A suitable choice for the boundary layer width is

$$\epsilon = (m_p \alpha)^{-\frac{1}{2}}, \qquad (53)$$

such that (52) can be rewritten as

$$\beta\frac{\partial^2 \varphi}{\partial \hat{x}^2} = \frac{\epsilon}{c} e^{-\varphi}\frac{\partial \varphi}{\partial \hat{t}} - e^{-\varphi}\frac{\partial \varphi}{\partial \hat{x}} - \frac{\epsilon}{c}\frac{\partial}{\partial \hat{t}}\left(\frac{\partial^2 \varphi}{\partial \hat{x}^2}\right) + \frac{\partial^3 \varphi}{\partial \hat{x}^3} \quad (54)$$

where the parameter β is defined by

$$\beta = \frac{\epsilon}{\lambda c}. \qquad (55)$$

Since we implicitly assume that $\epsilon \ll c$, both terms containing a time derivative can be neglected, to give the leading order balance in the inner region

$$\frac{d^3 \varphi}{d\hat{x}^3} - \beta\frac{d^2 \varphi}{d\hat{x}^2} - e^{-\varphi}\frac{d\varphi}{d\hat{x}} = 0 \qquad (56)$$

In order to match the solution to the right hand outer solution, we impose the matching condition $\varphi \to 0$ as
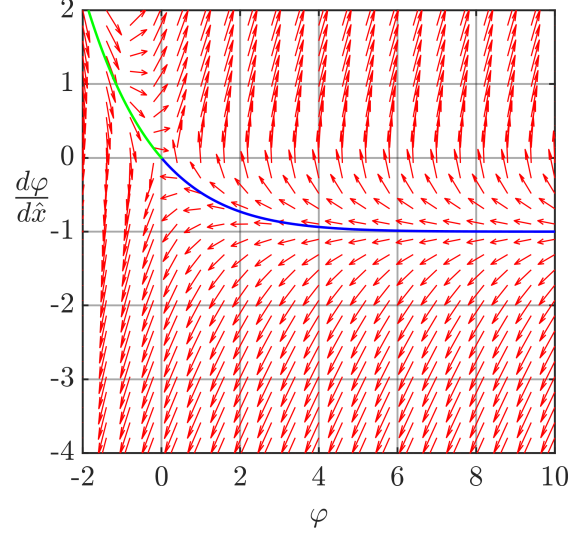

FIG. 9. Phase plane of the inner problem (57) where $\beta = 1$. Arrows show the direction of increasing $\hat{x}$. Solid lines show the two solutions that meet the right hand matching condition. Only the blue line can meet the left hand matching condition.

$\hat{x} \to \infty$. We integrate (56) once and apply this condition to obtain

$$\frac{d^2 \varphi}{d\hat{x}^2} - \beta\frac{d\varphi}{d\hat{x}} + e^{-\varphi} - 1 = 0. \qquad (57)$$

We now make use of a phase plane (Figure 9 shows an illustrative example for $\beta = 1$). Notably all phase planes with $\beta > 0$ exhibit the same qualitative features and exhibit two solutions that satisfy the right hand matching condition by terminating at the critical point $(\varphi, \frac{d\varphi}{d\hat{x}}) = (0, 0)$. However, the solution in the second quadrant (green curve in Fig. 9) becomes infinitely negative as $\hat{x} \to -\infty$, and so is clearly inconsistent with the left-hand boundary condition (which is positive for a reverse sweep). We therefore adopt the solution in the fourth quadrant (blue curve in Fig. 9). Matching to the left-hand outer solution and applying the boundary condition at $x = 0$ will identify β (and therefore c also) as a function of the sweep rate. As seen in the phase plane, the gradient $\frac{d\varphi}{d\hat{x}}$ tends toward a finite constant as $\hat{x} \to -\infty$, identifiable from (57) as $\frac{d\varphi}{d\hat{x}} \to \frac{-1}{\beta}$. Thus far, we have not defined the point $x = ct$ and therefore have the freedom to define it as the point at which the left-hand outer solution becomes zero, i.e. $\varphi^L|_{x=ct} = 0$. The far-field behaviour of the inner solution on the left hand side is therefore $\varphi \sim \frac{-\hat{x}}{\beta}$ as $\hat{x} \to -\infty$. On rewriting $\hat{x}$ in terms of outer coordinates and matching to the left-hand outer region, we see that the left-hand outer solution is, to leading order,

$$\varphi^L = \frac{1}{\epsilon\beta}(ct - x) \quad \text{for} \quad x < ct \qquad (58)$$

On imposing the boundary condition (47d) on $x = 0$, and

referring back to the definitions of ϵ and β ((53) and (55)), we obtain the following expression for the wavespeed

$$c = \frac{\psi_0(t)\epsilon\beta}{t} = \sqrt{\frac{\psi_0(t)}{m_p\alpha\lambda t}} \qquad (59)$$

We also note that the leading order outer electric field is given by

$$E^L(t) = \frac{1}{\epsilon\beta} = m_p\alpha c\lambda. \qquad (60)$$

It remains to relate the function $\psi_0(t)$ to the applied voltage, and to redimensionalise to obtain the wavespeed as a function of the material parameters.

The boundary condition (47e) contains a linear component corresponding to the applied voltage and two highly nonlinear components corresponding to the Debye layer potential drops, and begins from $\psi_0(0) = 0$. When the sweep rate is large, the sweep will finish before the Debye layers can discharge due to the slow nature of the ion motion, meaning ψ_0 is dominated by the change in applied voltage, and can be approximated by

$$\psi_0(t) \approx -\frac{d\Phi}{dt}t, \qquad (61)$$

where $\frac{d\Phi}{dt}$ is the (constant) sweep rate. At slower scan rates, the Debye layers have time to discharge but numerical simulations show that the wavefront typically crosses the layer faster than timescales of Debye layer discharge. For this reason, (61) is a valid approximation for slow scan rates during the time before the wavefront has crossed the layer. Under this approximation, the wavespeed (59) becomes a constant,

$$c = \sqrt{-\frac{d\Phi}{dt}\frac{1}{m_p\alpha\lambda}}. \qquad (62)$$

After reapplying the scalings in (44), we obtain the dimensional speed of the wavefront in terms of material parameters,

$$c_{\text{dim.}} = \sqrt{\frac{-D_P N_0 g_v^H}{V_T d_H g_v}\frac{dV}{dt}} \exp\left(\frac{V_3^{\text{pre}} + V_4^{\text{pre}} + E_v^H - E_v}{2V_T}\right). \qquad (63)$$

This approximation for the wavefront speed displays excellent agreement with the numerical solutions of the full three-layer drift-diffusion model obtained from `IonMonger`, as shown in Figure 10.

C. The effect of recombination on hysteresis

The travelling wave solution to the bulk electric potential problem divides the perovskite bulk into two regions: (I) ahead of the wavefront ($x > ct$), the electric field strength is negligible, and (II) behind the wavefront
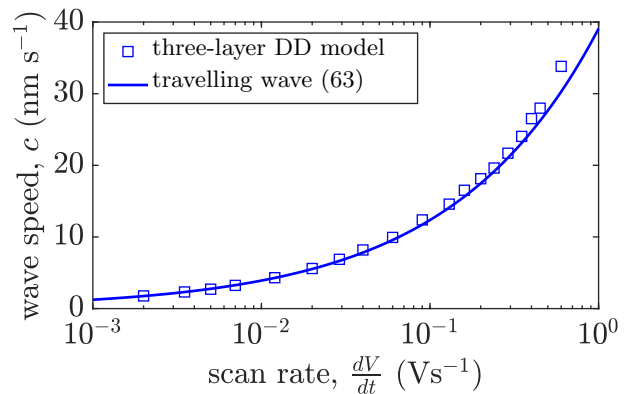

FIG. 10. Comparison between the travelling wavefront solution and the full three-layer DD model for wavefront speed across a range of experimentally relevant scan rates. Squares are data from numerical solutions using `IonMonger` and the solid line is the travelling wavefront solution (63).

($x < ct$), the electric field strength is strong and positive. In the first region, carrier distributions remain at their (approximately uniform) steady state distributions found during preconditioning with a large density of holes (given by (43)) and a much smaller density of electrons, as shown in Figure 11. Once the wavefront has passed through through a region however, the strong electric field quickly removes carriers, pushing them toward their respective transport layers for extraction. Both hole and electron densities are therefore small in this region.

The effect on the observed hysteresis of this wavefront is determined by the recombination parameters. Here we consider three distinct regimes: (i) hole-limited SRH recombination in the bulk; (ii) interfacial SRH recombination only; and (iii) a combination of the first and second types.

(i) Hole-limited bulk recombination When recombination in the perovskite bulk is strongly hole-limited ($\tau_p \gg \tau_n$), current losses occur in the hole-rich region ahead of the wavefront but not in the region behind, as shown in Figure 11, meaning performance is inhibited at the beginning of the sweep but recovers as the wavefront reaches the HTL interface, and the cell approaches short-circuit. In this scenario, $J_{\text{rev}} < J_{\text{for}}$ for most or all of the power-generating region, giving a negative hysteresis factor (37).

(ii) Interfacial recombination only When bulk recombination is neglected and interfacial recombination considered, the behaviour of the electric potential wavefront is unchanged but the resulting effect on the current density is significantly different. As the wavefront traverses the perovskite layer, generated carriers are no longer lost to bulk recombination but instead eventually drift or diffuse toward their respective transport layers. During this period therefore, current output is not inhibited by the wavefront. Once the wavefront has crossed the entire layer, however, the (now-uniform) electric field
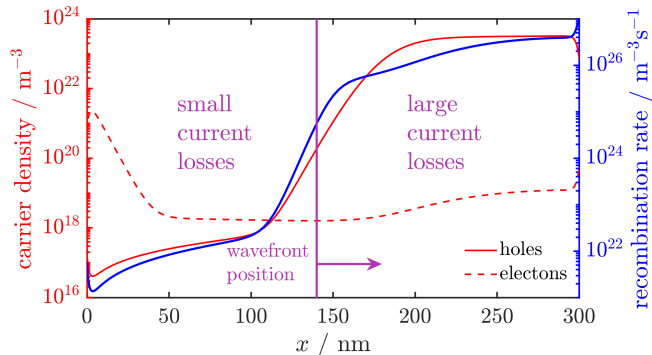
FIG. 11. Carrier densities (red) and bulk recombination rate (blue) in the perovskite layer at a point during the reverse sweep as calculated by `IonMonger`. Recombination parameters determine that bulk recombination is strongly hole-limited and interfacial recombination is neglected. The region of large current losses occupies the entire layer at the beginning of the sweep but recedes, resulting in the recovery of current density throughout the sweep symptomatic of IH.
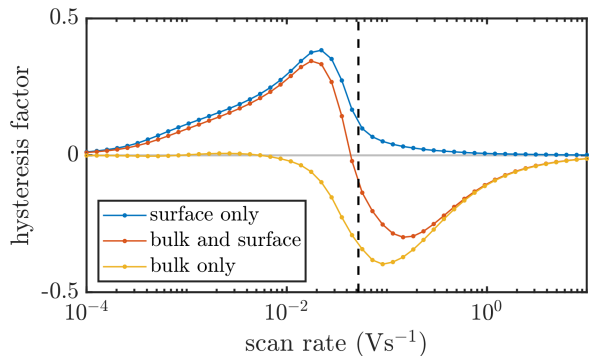

FIG. 12. Hysteresis factor as a function of scan rate under different recombination regimes. All simulations were performed in `IonMonger` using the parameter set in Table S1 with the recombination parameters in Table S2 of the Supplementary Information following preconditioning at 1.4V. All three simulations exhibit the same wavefront behaviour. The black dashed line is the scan rate, given by Eq. (64), at which normal hysteresis is predicted to switch to inverted hysteresis by the wavefront analysis.

in the perovskite bulk will eventually switch sign, driving carriers toward the wrong transport layers, resulting in large surface recombination losses at the interfaces. Current density is therefore inhibited only after the wavefront has completed its journey, resulting in a positive hysteresis factor ($J_{\mathrm{rev}} > J_{\mathrm{for}}$).

(iii) Interfacial and bulk recombination Introducing a combination of bulk and interfacial recombination leads to mixed normal and inverted hysteresis, as shown in Figure 12. At high scan rates, most or all of the sweep occurs before the wavefront has traversed the perovskite layer, leading to the bulk losses described in **(i)** that cause inverted hysteresis. At lower scan rates, however, most of the scan occurs after the wavefront has traversed the layer, causing the interfacial losses described in **(ii)** that cause normal hysteresis. This switchover from normal to inverted hysteresis as scan rate becomes higher has been observed experimentally [41, 42].

The scan rate at which the hysteresis switches from positive to negative can be related to material parameters using the wavefront analysis performed in the previous section. This scan rate is that at which the wavefront crosses the perovskite layer in the same time as taken for the reverse sweep, such that the bulk recombination losses occur on the reverse sweep and surface recombination losses on the forward sweep. Using the wavefront speed (63), this scan rate is found to be

$$\left| \frac{dV}{dt} \right| = \frac{D_P N_0 V_{\mathrm{pre}}^2 g_v^H}{V_T b^2 d_H g_v} \exp\left(\frac{V_3^{\mathrm{pre}} + V_4^{\mathrm{pre}} + E_v^H - E_v}{V_T} \right), \tag{64}$$

where V_{pre} is the voltage from which the sweep begins. At lower scan rates, the wavefront completes its journey before the cell reaches short-circuit, meaning most of the sweep is spent in the regime in which surface recombination, and therefore normal hysteresis, dominate. Similarly, at larger scan rates, the wavefront does not complete its journey until after the cell reaches short-circuit, meaning more time is spent in the region in which bulk recombination, and therefore inverted hysteresis, dominates. This prediction of the switchover scan rate is compared against solutions of the full DD model in Figure 12.

Whereas the timescales of hysteresis (normal or inverted) are determined by material parameters, the sign and magnitude of the hysteresis can signify the location and severity of the dominant recombination mechanism in the cell. A cell that shows inverted hysteresis across the full range of hysteretic scan rates is dominated by hole-limited bulk recombination, whereas the presence of a positive peak at a lower scan rate than the negative peak (as measured experimentally by Garcia-Rodriguez *et al.* [41]) indicates interfacial recombination where the relative sizes of the two peaks are determined by the relative magnitudes of the two recombination sources.

VI. CONCLUSIONS

In summary, an asymptotic analysis of the drift-diffusion model of a three-layer planar PSC has been used to show that a high density of one of the carriers inside the perovskite layer after preconditioning results in a wavefront (in electric potential) propagating across the perovskite layer during the reverse voltage sweep. The electric field propagates with this wavefront and therefore takes some time to permeate the entire perovskite layer, with the region ahead of the wavefront being diffusion-limited. If bulk recombination is strongly limited by the majority carrier in the perovskite, significant current losses occur in the region ahead of the front (where

the electric field is weak and there is a high density of majority carriers) and it is not until the wavefront has crossed the entire perovskite layer that the losses are reduced to a low level. This leads to the observation of inverted hysteresis since current losses are higher on the reverse sweep than the forward sweep that follows it.

This description of IH unifies the mechanisms proposed in the literature based upon numerical simulations of the DD model [39–41]. However, none of the explanations offered in these works provide a comprehensive explanation of the phenomenon. Plots of carrier density and recombination rate by García-Rodríguez *et al.* [41] exhibit the large variation between the regions in front of and behind the wavefront only for parameter sets that display inverted hysteresis but the movement of the wavefront across the layer or the conditions necessary for it to appear were not discussed. Similarly, the large preconditioning voltage found to be necessary by Jacobs *et al.* [39] is one way of inducing large hole populations in the perovskite due to the asymmetric extraction barriers caused by the capacitance relations of the Debye layers but, once again, the wavefront was not identified (perhaps due to the limitations of the model used). Unlike these works, Shen *et al.* [40] correctly identified the existence of a diffusion-limited region during sweeps that show inverted hysteresis as a result of significant accumulated charge in the bulk. This work has been built upon here by analysis of the evolution of this diffusion-limited region, linking timescales of inverted hysteresis to macroscopic material parameters. It has also been shown that, in principle, IH could be seen as a result of either electrons outnumbering holes or holes outnumbering electrons. However, preconditioning at large voltages presents a greater extraction barrier to holes than electrons, due to the asymmetry of the Debye layer capacitance relation , and the conclusions of Stranks *et al.* [49] suggest that SRH recombination in perovskites is typically hole-limited. Both of which suggest that holes outnumbering electrons is a far more likely scenario when inverted hysteresis is observed. The conditions that influence this are summarised in the next section.

Inverted hysteresis as a diagnostic tool

In recent years, interest in current-voltage hysteresis has begun to wane in the PSC community, due to its focus on pushing the PCE of 'champion' cells and the mistaken belief that hysteresis is only seen in poor cells [50] (for example, Refs. [51–53] report high performance cells that still exhibit hysteresis). However, in order to continue to increase the efficiency and stability of average cells, and the consistency across many batches, it is vital to develop our understanding of the internal mechanisms of devices.

The results of the modified SPM therefore suggest that observation of inverted hysteresis offers a glimpse into the limiting factor of a cell's performance and a chance to improve a cell's steady-state efficiency. The dimensionless constants that determine the influence of electrons and holes, respectively, on the electric potential in the perovskite (usually thought to be negligibly small in previous models) are defined in terms of dimensional material parameters as

$$m_n = \frac{d_E b^2 q g_c}{V_T \varepsilon_p g_c^E} \exp\left(\frac{E_c^E - E_c}{k_B T}\right), \qquad (65a)$$

$$m_p = \frac{d_H b^2 q g_v}{V_T \varepsilon_p g_v^H} \exp\left(\frac{E_v - E_v^H}{k_B T}\right). \qquad (65b)$$

The exponential dependence of these constants on transport layer band offsets suggests that these are the material properties to which inverted hysteresis (and the large carrier densities of which it is symptomatic) is most sensitive. Therefore, if inverted hysteresis is still observed when the preconditioning voltage is decreased, approaching V_{OC}, it is likely that one of the transport layer band offsets is insufficient for efficient carrier extraction and the cell could be improved by substitution of an alternative transport layer material that forms a greater band offset with the perovskite. Furthermore, the magnitude of inverted hysteresis has been shown to indicate the level of bulk recombination occurring in the cell, with the magnitude of normal hysteresis indicating the corresponding level of surface recombination occurring at the interfaces. Together, these observations from the modified SPM provide a pathway to improve the stabilised efficiency of a cell that displays inverted hysteresis.

ACKNOWLEDGMENTS

[1] J. J. Yoo, G. Seo, M. R. Chua, T. G. Park, Y. Lu, *et al.*, Nature **590**, 587 (2021).

[2] H.-S. Kim, C.-R. Lee, J.-H. Im, K.-B. Lee, T. Moehl, *et al.*, Scientific Reports **2**, 10.1038/srep00591 (2012).

[3] M. M. Lee, J. Teuscher, T. Miyasaka, T. N. Murakami, and H. J. Snaith, Science **338**, 643 (2012).

[4] NREL, Best research-cell efficiency chart, `https://www.nrel.gov/pv/cell-efficiency.html` (accessed

08/04/2022).

[5] G. E. Eperon, V. M. Burlakov, P. Docampo, A. Goriely, and H. J. Snaith, Advanced Functional Materials **24**, 151 (2014).

[6] Z. Xiao, C. Bi, Y. Shao, Q. Dong, Q. Wang, *et al.*, Energy Environ. Sci. **7**, 2619 (2014).

[7] M. Liu, M. B. Johnston, and H. J. Snaith, Nature **501**, 395 (2013).

[8] K. Wojciechowski, M. Saliba, T. Leijtens, A. Abate, and H. J. Snaith, Energy Environ. Sci. **7**, 1142 (2014).

[9] Oxford PV, (2021), `https://www.oxfordpv.com/news/oxford-pv-completes-build-out-its-brandenburg-factory` Accessed 03/08/2022.

[10] H. J. Snaith, Nature Materials **17**, 372 (2018).

[11] A. Babayigit, A. Ethirajan, M. Muller, and B. Conings, Nature Materials **15**, 247 (2016).

[12] H. J. Snaith, A. Abate, J. M. Ball, G. E. Eperon, T. Leijtens, *et al.*, The Journal of Physical Chemistry Letters **5**, 1511 (2014).

[13] J. M. Cave, N. E. Courtier, I. A. Blakborn, T. W. Jones, D. Ghosh, K. F. Anderson, L. Lin, A. A. Dijkhoff, G. J. Wilson, K. Feron, M. Saiful Islam, J. M. Foster, G. Richardson, and A. B. Walker, Journal of Applied Physics **128**, 184501 (2020).

[14] S. Van Reenen, M. Kemerink, and H. J. Snaith, The Journal of Physical Chemistry Letters **6**, 3808 (2015).

[15] G. Richardson, S. E. J. O'Kane, R. G. Niemann, T. A. Peltola, J. M. Foster, P. J. Cameron, and A. B. Walker, Energy & Environmental Science **9**, 1476 (2016).

[16] N. E. Courtier, J. M. Cave, J. M. Foster, A. B. Walker, and G. Richardson, Energy & Environmental Science **12**, 396 (2019).

[17] A. Riquelme, L. J. Bennett, N. E. Courtier, M. J. Wolf, L. Contreras-Bernal, *et al.*, Nanoscale **12**, 17385 (2020).

[18] N. Tessler and Y. Vaynzof, ACS Energy Letters **5**, 1260 (2020).

[19] J. Wei, Y. Zhao, H. Li, G. Li, J. Pan, *et al.*, The Journal of Physical Chemistry Letters **5**, 3937 (2014).

[20] J. M. Frost, K. T. Butler, and A. Walsh, APL Materials **2**, 081506 (2014).

[21] C. Li, S. Tscheuschner, F. Paulus, P. E. Hopkinson, J. Kießling, *et al.*, Advanced Materials **28**, 2446 (2016).

[22] C. Eames, J. M. Frost, P. R. F. Barnes, B. C. O'Regan, A. Walsh, *et al.*, Nature Communications **6**, 7497 (2015).

[23] C. Jacoboni, *Theory of electron transport in semiconductors: a pathway from elementary physics to nonequilibrium Green functions*, Vol. 165 (Springer Science & Business Media, 2010).

[24] T. Grasser, T. Ting-Wei, H. Kosina, and S. Selberherr, Proceedings of the IEEE **91**, 251 (2003).

[25] P. Calado, A. M. Telford, D. Bryant, X. Li, J. Nelson, B. C. O'Regan, and P. R. Barnes, Nature communications **7**, 1 (2016).

[26] N. E. Courtier, G. Richardson, and J. M. Foster, Applied Mathematical Modelling **63**, 329 (2018).

[27] P. Calado, I. Gelmetti, B. Hilton, M. Azzouzi, J. Nelson, and P. R. F. Barnes, Journal of Computational Electronics 10.1007/s10825-021-01827-z (2022).

[28] N. E. Courtier, J. M. Cave, A. B. Walker, G. Richardson, and J. M. Foster, Journal of Computational Electronics **18**, 1435 (2019).

[29] N. E. Courtier, J. M. Foster, S. E. J. O'Kane, A. B. Walker, and G. Richardson, European Journal of Applied Mathematics **30**, 427 (2019).

[30] S. Ravishankar, O. Almora, C. Echeverría-Arrondo, E. Ghahremanirad, C. Aranda, A. Guerrero, F. Fabregat-Santiago, A. Zaban, G. Garcia-Belmonte, and J. Bisquert, The Journal of Physical Chemistry Letters **8**, 915 (2017).

[31] D. Moia, I. Gelmetti, P. Calado, W. Fisher, M. Stringer, O. Game, Y. Hu, P. Docampo, D. Lidzey, E. Palomares, J. Nelson, and P. R. F. Barnes, Energy & Environmental Science **12**, 1296 (2019).

[32] L. Bertoluzzi, C. C. Boyd, N. Rolston, J. Xu, R. Prasanna, B. C. O'Regan, and M. D. McGehee, Joule **4**, 109 (2020).

[33] W. Tress, J. P. Correa Baena, M. Saliba, A. Abate, and M. Graetzel, Advanced Energy Materials **6**, 1600396 (2016).

[34] Y. Rong, Y. Hu, S. Ravishankar, H. Liu, X. Hou, *et al.*, Energy & Environmental Science **10**, 2383 (2017).

[35] E. Jokar, H.-S. Chuang, C.-H. Kuan, H.-P. Wu, C.-H. Hou, J.-J. Shyue, and E. Wei-Guang Diau, The Journal of Physical Chemistry Letters **12**, 10106 (2021).

[36] G. A. Nemnes, C. Besleaga, V. Stancu, D. E. Dogaru, L. N. Leonat, *et al.*, The Journal of Physical Chemistry C **121**, 11207 (2017).

[37] F. Wu, R. Pathak, K. Chen, G. Wang, B. Bahrami, *et al.*, ACS Energy Letters **3**, 2457 (2018).

[38] N. E. Courtier, *Modelling ion migration and charge carrier transport in planar perovskite solar cells*, Thesis, School of Mathematical Sciences, University of Southampton (2019).

[39] D. A. Jacobs, Y. Wu, H. Shen, C. Barugkin, F. J. Beck, *et al.*, Physical Chemistry Chemical Physics **19**, 3094 (2017).

[40] H. Shen, D. A. Jacobs, Y. Wu, T. Duong, J. Peng, *et al.*, The Journal of Physical Chemistry Letters **8**, 2672 (2017).

[41] R. García-Rodríguez, A. J. Riquelme, M. Cowley, K. Valadez-Villalobos, G. Oskam, L. J. Bennett, M. J. Wolf, L. Contreras-Bernal, P. J. Cameron, A. B. Walker, and J. A. Anta, Energy Technology 10.1002/ente.202200507 (2022).

[42] C. Gonzales, A. Guerrero, and J. Bisquert, The Journal of Physical Chemistry C **126**, 13560 (2022).

[43] J. Bisquert, A. Guerrero, and C. Gonzales, ACS Physical Chemistry Au **1**, 25 (2021).

[44] M. Minbashi and E. Yazdani, Scientific Reports **12**, 1 (2022).

[45] D. Abdel, P. Vágner, J. Fuhrmann, and P. Farrell, Electrochimica Acta **390**, 138696 (2021).

[46] A. Castro-Chong, A. J. Riquelme, T. Aernouts, L. J. Bennett, G. Richardson, *et al.*, ChemPlusChem **86**, 1347 (2021).

[47] M. T. Neukom, A. Schiller, S. Züfle, E. Knapp, J. Ávila, *et al.*, ACS Applied Materials & Interfaces **11**, 23320 (2019).

[48] S. N. Habisreutinger, N. K. Noel, and H. J. Snaith, ACS Energy Letters **3**, 2472 (2018).

[49] S. D. Stranks, V. M. Burlakov, T. Leijtens, J. M. Ball, A. Goriely, *et al.*, Physical Review Applied **2**, 10.1103/physrevapplied.2.034007 (2014).

[50] D. Bryant, S. Wheeler, B. C. O'Regan, T. Watson, P. R. F. Barnes, D. Worsley, and J. Durrant, The Journal of Physical Chemistry Letters **6**, 3190 (2015).

[51] X. Wang, K. Rakstys, K. Jack, H. Jin, J. Lai, H. Li,

C. S. K. Ranasinghe, J. Saghaei, G. Zhang, P. L. Burn, I. R. Gentle, and P. E. Shaw, Nature Communications **12**, 10.1038/s41467-020-20272-3 (2021).

[52] E. Aydin, J. Liu, E. Ugur, R. Azmi, G. T. Harrison, Y. Hou, B. Chen, S. Zhumagali, M. De Bastiani, M. Wang, W. Raja, T. G. Allen, A. U. Rehman, A. S. Subbiah, M. Babics, A. Babayigit, F. H. Isikgor, K. Wang, E. Van Kerschaver, L. Tsetseris, E. H. Sargent, F. Laquai, and S. De Wolf, Energy & Environmental Science **14**, 4377 (2021).

[53] Y. Zhang and N.-G. Park, ACS Energy Letters **7**, 757 (2022).